



Toward feasible single atom-based hydrogen evolution electrocatalysts via artificial ensemble sites for anion exchange membrane water electrolyzer

Won-Gwang Lim^{a,1,2}, Hoang Nam Truong^{b,1}, Jae-Yeop Jeong^{c,d,1}, Dongkyu Kim^{e,f},
Lee Seul Oh^{e,f}, Changshin Jo^g, Chiho Kim^c, Hyung Ju Kim^e, Sung Mook Choi^{c,h,*},
Hyeyoung Shin^{b,**}, Seonggyu Lee^{i,j,***}, Eunho Lim^{e,**}

^a Department of Chemical and Biomolecular Engineering, Korea Advanced Institute of Science and Technology (KAIST), 291 Daehak-Ro, Yuseong-Gu, Daejeon 34141, Republic of Korea

^b Graduate School of Energy Science and Technology (GEST), Chungnam National University, Daejeon 34134, Republic of Korea

^c Department of Hydrogen Energy Materials, Surface & Nano Materials Division, Korea Institute of Materials Science (KIMS), Changwon 51508, Republic of Korea

^d Department of Materials Science and Engineering, Pusan National University, Busan 46241, Republic of Korea

^e Chemical & Process Research Division, Korea Research Institute of Chemical Technology (KRICT), 141 Gajeongro, Daejeon 34114, Republic of Korea

^f Department of Chemical and Biomolecular Engineering, Yonsei University, 50 Yonsei-ro, Seoul 03722, Republic of Korea

^g Graduate Institute of Ferrous & Eco Materials Technology (GIFT) and Department of Chemical Engineering, Pohang University of Science and Technology (POSTECH), Pohang 37637, Republic of Korea

^h Advanced Materials Engineering, University of Science and Technology (UST), Daejeon 34113, Republic of Korea

ⁱ Department of Chemical Engineering, Kumoh National Institute of Technology (KIT), 61 Daehak-ro, Gumi 39177, Gyeongbuk, Republic of Korea

^j Department of Energy Engineering Convergence, Kumoh National Institute of Technology (KIT), 61 Daehak-ro, Gumi 39177, Gyeongbuk, Republic of Korea

ARTICLE INFO

Keywords:

Alkaline hydrogen evolution reaction
Artificial ensemble site
Single atom electrocatalyst
Water dissociation
Anion exchange membrane water electrolyzer

ABSTRACT

Approaching an efficient anion exchange membrane water electrolyzer (AEMWE) with satisfactorily high kinetics in the alkaline hydrogen evolution reaction (HER) is desired. We design an advanced platinum (Pt) single atom (SA)-based electrocatalyst by incorporating the Ni nanoparticle as an artificial ensemble site adjacent to Pt SA. The designed Pt SA electrocatalyst achieves higher areal current density (500 mA cm^{-2} at 1.8 V) in the single cell of the AEMWE and better cell voltage stability than the Pt/C electrocatalyst. The Ni nanoparticle assists in separating the binding sites of H^* and OH^* , in which Ni atoms provide adsorption sites for H^* , while OH^* adsorbs on the Pt SA. This separation effect drastically accelerates the energy barrier required for the water dissociation reaction in the Volmer step and simultaneously optimizes the H^* and OH^* binding energy, which extremely enhances the alkaline HER kinetics, thereby demonstrating the feasibility of Pt SA electrocatalysts for AEMWE.

1. Introduction

Hydrogen (H_2) is a promising sustainable energy carrier, poised to address the pressing challenge of carbon emissions [1–4]. The electrocatalytic H_2 evolution reaction (HER) via water splitting in alkaline media has been regarded as an essential prerequisite of the eco-friendly H_2 production over the years [5–7] because the alkaline HER has many

merits, including a long-term system lifetime and a large number of electrocatalyst candidates, whereas an acidic HER shows significantly poor durability and there are limitations on the number of efficient electrocatalysts which can be used [8–14]. Despite the several advantages, however, HER kinetics in alkaline media is a few orders of magnitude lower than in acidic media, which shows the large overpotential and limits the current density [15–18]. Therefore, in-depth

* Corresponding author at: Department of Hydrogen Energy Materials, Surface & Nano Materials Division, Korea Institute of Materials Science (KIMS), Changwon 51508, Republic of Korea.

** Corresponding authors.

*** Corresponding author at: Department of Chemical Engineering, Kumoh National Institute of Technology (KIT), 61 Daehak-ro, Gumi 39177, Gyeongbuk, Republic of Korea.

E-mail addresses: akyzaky@kims.re.kr (S.M. Choi), shinhy@cnu.ac.kr (H. Shin), seonggyulee@kumoh.ac.kr (S. Lee), eunholim@kRICT.re.kr (E. Lim).

¹ These authors contributed equally to this work.

² Present address: Energy and Environment Directorate, Pacific Northwest National Laboratory, Richland, WA 99354, USA

studies of developing advanced electrocatalysts to enhance the sluggish kinetics of HER in alkaline media are necessary to achieve energy-efficient H_2 production.

Though platinum (Pt) is one of the most powerful electrocatalysts for the HER in alkaline environments due to its relatively more favorable hydrogen binding behaviors compared to other electrocatalysts [19–24], its widespread commercial application in water electrolyzers is impeded by its high cost and scarcity. Therefore, Pt single atom (SA)-based electrocatalysts have emerged as a promising strategy to maximize Pt utilization efficiency [25–28], decrease overpotential, and consequently reduce Pt consumption [29,30]. Numerous precedent studies have made significant improvements in HER kinetics by

designing Pt SA-based electrocatalysts through a multifaceted approach (e.g., increasing the amounts of Pt SA [31,32] and modulating Pt *d*-orbital level [33]). However, despite intensive efforts, several challenges remain for the development of advanced Pt SA-based electrocatalysts for alkaline HER.

Especially in the alkaline HER, the dissociation behavior of water is of significant importance, as water serves as the sole proton source required to initiate the hydrogen evolution [34,35]. Nevertheless, the energy barrier for dissociating the strong OH–H bonds of water molecules into H^* and OH^* (i.e., the Volmer step) on the Pt SA electrocatalyst is still not sufficiently low, which thereby limits the further improvement of the kinetics of alkaline HER. Furthermore, in order to sustain a

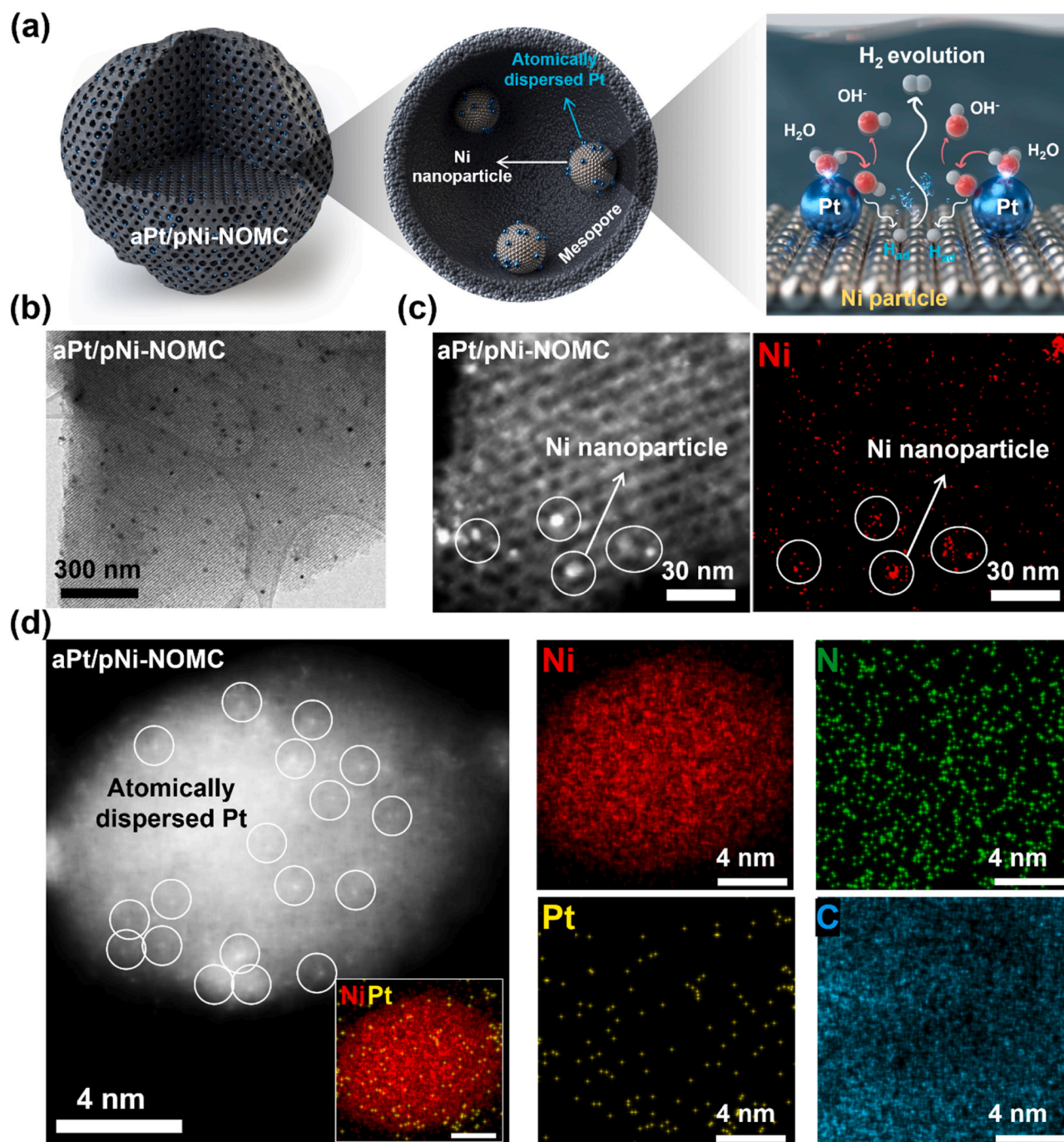


Fig. 1. (a) Schematics of the as-prepared aPt/pNi-NOMC electrocatalyst and its effect on the alkaline HER. (b) Low-magnification TEM, (c) HAADF-STEM and EDS mapping images of aPt/pNi-NOMC. (d) High-resolution HAADF-STEM and EDS mapping images of aPt/pNi-NOMC. The scale bar of the inset EDS mapping image is 4 nm.

continuous HER at the active sites, efficient desorption of dissociated H^* and OH^* is necessary, and it is governed by appropriate hydrogen binding energy (HBE) and hydroxide binding energy (OHBE) [9,36,37]. However, the simultaneous optimization of both HBE and OHBE on the active sites of the Pt SA electrocatalyst is intrinsically restricted because Pt SA has only one atomic site for the adsorption of both H^* and OH^* , which thus limits effective control over the adsorption behaviors of these two different reaction intermediates. In this regard, the design of advanced Pt SA-based electrocatalysts that satisfy both a significantly low energy barrier for the water dissociation at the Volmer step and also simultaneously optimizes HBE and OHBE is necessary for pushing the kinetics of alkaline HER to the next stage.

Furthermore, in order to assess the feasibility of the Pt SA-based electrocatalyst, it is crucial to investigate its performance in a zero-gap membrane electrode assembly (MEA) of an anion exchange membrane water electrolyzer (AEMWE) single cell with high current densities exceeding 500 mA cm^{-2} . However, the most of the previously reported Pt SA-based electrocatalysts have only been evaluated at the three-electrode system-based half cells. Particularly with regard to Pt SA-based electrocatalysts, the substantial increase in catalyst layer thickness due to the low Pt density within the electrocatalyst (in terms of weight percentage) can result in a notable decrease in the performance of AEMWEs. This decline in performance significantly hinders the feasibility of their practical application. Therefore, it is imperative not only to enhance the kinetic activity of Pt SA-based electrocatalysts, but also to develop strategies for improving the performance of the MEA of AEMWE single cell.

Here, we propose a novel concept to design advanced Pt SA-based electrocatalysts to enhance the kinetics of the HER in alkaline media by atomically separating the H^* and OH^* binding sites. We developed Pt electrocatalysts atomically dispersed on the surface of Ni nanoparticles which are supported by a N-doped ordered mesoporous carbon (NOMC) substrate (aPt/pNi-NOMC, 'a' and 'p' represent the physical state of atomically dispersed Pt and particle-type Ni, respectively) (Fig. 1a). The designed aPt/pNi-NOMC showed a separated adsorption of H^* and OH^* intermediates on two different sites. Ni atoms adjacent to a Pt SA can act as a binding site of H^* species, whereas OH^* adsorbs on the surface of the Pt SA. This atomic separation of H^* binding site by Ni nanoparticle leads to i) the drastic decrease of the energy barrier required for dissociating the strong $\text{OH}-\text{H}$ bonding of water molecules in the Volmer step and ii) simultaneous optimization of HBE and OHBE on the surface of Ni nanoparticles and Pt SA, respectively. Consequently, these specially designed aPt/pNi-NOMC electrocatalysts exhibited even lower overpotential at 100 mA cm^{-2} and 11 times higher mass activity at -0.2 V (vs. RHE) than 40 wt% Pt/C electrocatalysts in the half cell. More importantly, the AEMWE single cell with an aPt/pNi-NOMC cathode electrocatalyst showed a higher areal current density (500 mA cm^{-2} at 1.8 V) and a more stable cell voltage retention ratio at 500 mA cm^{-2} than the AEMWE single cell with a Pt/C electrocatalyst.

2. Experimental

2.1. Materials

Tetraethyl orthosilicate (TEOS), Pluronic F127, hydrochloric acid solution (HCl, concentration of 35–37%), urea (99.0%), chloroplatinic acid hexahydrate ($\geq 37.50\%$), acetone (99.9%), and nickel nitrate hexahydrate were purchased from Sigma-Aldrich. Anhydrous ethyl alcohol (EtOH), 2-propanol (IPA, 99.5%), hydrofluoric acid (HF, concentration of 49%), and 1.0 M KOH were purchased from Samchun Chemical. Nafion® solution (5 wt%, D521) was purchased from Dupont. Resol was synthesized via an amphiphilic surfactant templating method [38] and used as a carbon precursor. Commercial Pt/C and Ni/C (10, 20, and 40 wt%), which was used as a control group, were purchased from Premetek.

2.2. Synthesis of NOMC

NOMC was synthesized by an evaporation-induced self-assembly (EISA) method [39] using TEOS (silica precursor) and F127 (structure directing agent), followed by thermal decomposition of urea. First, 19 g of resol was dissolved in 94 mL of EtOH to prepare a homogeneous resol solution, and 42 mL of TEOS was added to the resol solution. Second, 30 g of F127 was dissolved in 188 mL of EtOH to prepare the homogeneous F127 solution. Then, 19 mL of 0.2 M HCl was added to the F127 solution drop wise and stirred for 1 h at 45°C . Third, the resol solution was added to the F127 solution and stirred for 2 h to induce a sol-gel reaction. Then the solution was poured into a petri dish and the temperature of the hot plate was fixed to 40°C to slowly evaporate the solvent. After removal of the solvent at 40°C , the petri dish was further annealed at 100°C overnight. The as-made sample was heat-treated at 350°C for 3 h and followed by 900°C for 2 h under an argon gas flow to complete the preparation of the ordered mesoporous carbon silica (OMCS) composite. The heating rate was controlled to 1°C min^{-1} up to 600°C and 5°C min^{-1} for $600-900^\circ\text{C}$. The OMCS was etched using a solution of HF, EtOH, and DI-water to completely remove the silica. After being washed several times with DI-water, the ordered mesoporous carbon (OMC) was dried in a vacuum oven overnight. Then, 10 g of as-prepared OMC was physically mixed with 15 g of urea to perform the soft-nitriding process [40]. The homogeneous mixture of OMC and urea was heat-treated at 150°C for 2 h, followed by 300°C for 2 h in a box furnace with a heating rate of 5°C min^{-1} . After being washed several times with DI-water, the NOMC was dried in a vacuum oven overnight.

2.3. Synthesis of pNi-NOMC, aPt-NOMC, and aPt/pNi-NOMC

The pNi-NOMC and aPt-NOMC electrocatalysts were synthesized by a wet impregnation method. For synthesis of pNi-NOMC, 1.6 g of nickel nitrate hexahydrate was dissolved in 18 mL of DI-water. This solution was dropped onto 6 g of NOMC and impregnated by grinding in a mortar. The mixture of nickel nitrate hexahydrate and NOMC was dried in a vacuum oven at 60°C overnight. Then, the dried powder was heat-treated at 550°C for 2 h under a 4% H_2/Ar gas flow with a heating rate of 1°C min^{-1} . The targeted Ni amount of pNi-NOMC electrocatalyst was 5 wt%. For synthesis of aPt/pNi-NOMC, 1.677 g of chloroplatinic acid hexahydrate was dissolved in 36 mL of anhydrous acetone. The 15 mL of this chloroplatinic acid hexahydrate solution was dropped onto 5 g of pNi-NOMC powder and impregnated by grinding in a mortar. The mixture of the pNi-NOMC and Pt precursor was dried in a vacuum oven at 60°C overnight. Then, the dried powder was heat-treated at 150°C with heating rate of $0.6^\circ\text{C min}^{-1}$ under a 4% H_2/Ar gas flow and followed by 200°C with a heating rate of $0.6^\circ\text{C min}^{-1}$ under a H_2 gas flow for 2 h. Then, it was cooled down to room temperature under a N_2 gas flow. The targeted Pt amount of aPt/pNi-NOMC electrocatalyst was 5 wt%. The aPt-NOMC was synthesized by same method as that of aPt/pNi-NOMC, but by using NOMC instead of pNi-NOMC.

2.4. Material characterization

To characterize the crystal structure of each electrocatalyst, we used X-ray diffraction (XRD, Rigaku D/Max 2200 V, $\text{Cu K}\alpha$ radiation) analysis. We also performed N_2 adsorption-desorption analysis (Micromeritics ASAP 2420) at 77 K to investigate the porous architectures of the as-prepared electrocatalysts. To characterize the valence state of the electrocatalysts, X-ray photoelectron spectroscopy (XPS, Thermo Fisher Scientific K-Alpha+ XPS) was carried out. We studied the detailed electronic structures of each electrocatalyst by X-ray absorption spectroscopy (XAS) analysis using a 7D XAFS beamline at the Pohang Accelerator Laboratory (PAL, Republic of Korea). Scanning electron microscopy (SEM, Tescan Mira3 LMU, transmission electron microscopy (TEM, Thermo Fisher Scientific Talos F200S) and spherical aberration-

corrected TEM (Cs-TEM, FEI Titan cubed G2 60–300) were used to investigate the particle morphology of the electrocatalysts. The elemental mappings were performed by energy dispersive X-ray spectrometer (EDS) attached to the TEM equipment. The metal content of the electrocatalysts was analyzed by inductively coupled plasma optical emission spectrometer (ICP-OES, Agilent ICP-OES 720).

2.5. Electrochemical measurements

The 8 mg of as-prepared electrocatalyst (aPt/pNi-NOMC, aPt-NOMC, pNi-NOMC, and 10, 20, 40 wt% Pt/C) was dispersed in 0.4 mL of DI-water and 1.6 mL of IPA. The 0.045 mL of Nafion® solution was added to the electrocatalyst solution and followed by the sonication for 30 min. The 10 μ L of this electrocatalyst ink was dropped on a glassy carbon electrode (GCE, 5 mm diameter) and dried at room temperature. The electrocatalyst loading on the GCE corresponds to 0.1993 mg cm_{geo}⁻² (geo: geometric area of GCE). The detailed areal loading amounts of Pt and Ni are described in Table S6. The GCE was used as a working electrode, whereas graphite and Hg/HgO (1.0 M NaOH) electrodes were used as counter and reference electrodes, respectively. A 1.0 M KOH solution was used as the electrolyte and purged by H₂ gas for 30 min before cell testing. For the calibration of the reference electrode, the Pt rotating disk electrode (RDE, 5 mm diameter) and Pt wire were used as working and counter electrodes, respectively, in a H₂-saturated 1.0 M KOH electrolyte. The calibration resulted in a shift of -0.920 V (vs. RHE) for the 1.0 M KOH solution. All potential values were calibrated to the reversible hydrogen electrode (RHE) using $E(\text{RHE}) = E_{\text{Hg/HgO}} + 0.920 \text{ V}$. The rotating rate of the RDE was controlled to 1600 rpm. A linear sweep voltammetry (LSV) test was performed at a scan rate of 5 mV s⁻¹ and a chronopotentiometry test was performed at a current density of 10 mA cm_{geo}⁻² using a potentiostat (ZIVE MP1, WonATech). An accelerated durability test (ADT) indicates the LSV test after the cyclic voltammetry (CV) test for 1000 cycles at the scan rate of 100 mV s⁻¹. Electrochemical impedance spectroscopy (EIS) was performed at -0.1 V (vs. RHE) in the frequency range of 10⁻¹–10⁵ Hz with a potential amplitude of 5 mV. The mass activity indicates the activity per total mass of Pt (A mg_{Pt}⁻¹). The electrochemical surface area (ECSA) of Pt was determined by assessing the feature related to hydrogen underpotential deposition (H_{upd}). The CV for the ECSA was acquired within the potential range of 0.05–1.20 V (vs. RHE), using a scan rate of 50 mV s⁻¹. The ECSA was computed using the following equation [33,41].

$$\text{ECSA}(\text{m}^2 \text{ g}^{-1}_{\text{Pt}}) = \frac{Q_{\text{H}}}{q \times [\text{Pt}]}$$

where Q_{H} represents the charge associated with hydrogen desorption, q denotes the monolayer hydrogen desorption charge (210 $\mu\text{C cm}^{-2}$), and $[\text{Pt}]$ signifies the total amount of Pt loaded on the electrode.

2.6. Configuration and characterization of AEMWE single cell

The AEMWE single cell, designed to assess the performance of synthesized electrocatalysts, is composed of an anode (electrode size: 7.065 cm²), a cathode (electrode size: 4.9 cm²), an anion exchange membrane (AEM, X37–50 grade T, Dioxide), a membrane electrode assembly (MEA) holder, Ni foam (NF, Alantum, pore size: 450 μ m) as a porous transport layer (PTL), a stainless steel current collector, and an end plate (Fig. 6a and S25). The active area of the AEMWE single cell is 4.9 cm². Electrochemical analyses of the AEMWE single cells were conducted using a potentiostat (VSP, BioLogic) equipped with a high current booster (20 A, BioLogic). The polarization curves of the AEMWE single cells were obtained by measuring the cell voltage (V_{cell}) in the range of 1.3–1.95 V at a scan rate of 1 mV s⁻¹. The operational temperatures of the AEMWE single cells were 45, 60, and 75 °C, respectively. The durability of the AEMWE single cells was evaluated for 210 h under the conditions of 45 °C, a 0.1 M KOH electrolyte, and a constant

current density of 500 mA cm⁻². The developed aPt/pNi-NOMC electrocatalyst was fabricated as a HER electrode through the ultrasonic spray coating method on carbon cloth and used as the cathode. The ink solution was prepared by dispersing aPt/pNi-NOMC (500 mg), IPA (10 g, 70.0%), and a 5 wt% Nafion solution (2.5 g) in DI-water (3 g) using ultrasonication for 10 min. The loading amount of Pt was approximately 0.5 mg cm⁻². For a comparison with commercial Pt-based HER electrocatalysts, an electrode coated with 10 and 40 wt% Pt/C on a carbon cloth were prepared. The ink solution for the 10 and 40 wt% Pt/C electrode was prepared using the same solution composition as the ink solution for aPt/pNi-NOMC. However, 10 and 40 wt% Pt/C (500 mg) were used instead of aPt/pNi-NOMC. To fabricate the anode of the AEMWE single cell, composite electrocatalysts of Co₃O₄ and Ni foam (Co₃O₄/NF) were prepared following the procedure outlined in our previous paper [42]. However, to minimize the variables introduced by the anode, the Co₃O₄/NF electrocatalyst was fabricated using the precipitation method with only a cobalt precursor (0.1 M) instead of co-precipitation of copper and cobalt.

2.7. Computational details

Spin-polarized density functional theory (DFT) calculations were performed using the Vienna Ab initio Software Package (VASP) program [43]. The Perdew–Burke–Ernzerhof (PBE) functional [44] was employed and the long-range dispersion interactions were corrected using the D3 method [45,46]. The projector augmented wave (PAW) pseudopotentials were used to describe the electron-ion interactions [47]. For the geometry optimization, the plane-wave energy cutoff was set to 520 eV, and all geometries were relaxed to their ground state using a conjugate gradient algorithm [48] with an energy convergence criterion of 0.0001 eV Å⁻¹. To represent experiments more accurately in aqueous conditions, the implicit solvation model employing the Poisson–Boltzmann solver was utilized as implemented in VASPsol [49]. For the bulk structure of Ni, a face-centered cubic crystal unit cell was used. A (7×7×7) Monkhorst-Pack k-point grid was employed for the optimization of Ni bulk, and the calculated lattice constant for Ni bulk (3.46 Å) was found to be in good agreement with the experimental value of 3.52 Å. For the pNi and NOMC surfaces, a (2×2) Ni slab model consisting of four atomic layers and a (4×4) N-doped graphene slab model containing 31 C atoms and 1 N atom were used, respectively. For the construction of the aPt/pNi and aPt-NOMC slab models, all possible adsorption sites for Pt on both pristine pNi and NOMC surface models were considered as illustrated in Fig. S23a and b, and we selected the most stable Pt adsorption models on each surface for further discussion (see Fig. S24a and b). For all surface models, the Brillouin zone was sampled with a (7×7×1) Monkhorst-Pack k-point grid. During the geometry optimization, the top three layers, including the adsorbates, were relaxed, while the bottom layer was kept fixed at its bulk position. The Gibbs free energy (G) for each step of the overall reaction mechanism was calculated by considering the total electronic energy, solvation energy, zero-point energy, and entropy. For the adsorption free energy calculation of H₂O and OH, all possible adsorption sites on each surface were considered (Fig. S23a, c and d). To calculate the kinetic barrier for the water dissociation, transition states were searched using the nudged elastic band (NEB) method [50,51], with a force convergence criterion of 0.05 eV Å⁻¹.

3. Results and discussion

3.1. Design of aPt/pNi-NOMC electrocatalyst

Considering that electrically conductive support materials with high surface area and facile transport of reactants is indeed of great importance in the design of highly active Pt SA-based electrocatalysts [52], NOMC with a suitable porous architecture was prepared as a support material of an aPt/pNi-NOMC electrocatalyst. TEM images of NOMC

prepared by an EISA method revealed homogeneously well-developed cylindrical mesopores (Fig. S1). The N_2 physisorption analysis of NOMC showed a type-IV isotherm linear plot with significant capillary condensation behavior at a P/P_0 of ~ 0.6 , which suggests the presence of mesopores (Fig. S2a). The Brunauer-Emmett-Teller (BET) specific surface area and pore volume of NOMC are $1151 \text{ m}^2 \text{ g}^{-1}$ and $1.3 \text{ cm}^3 \text{ g}^{-1}$, respectively. The Barrett-Joyner-Halenda (BJH) pore size distribution of NOMC was obviously centered at 5.7 nm, which was consistent with the TEM analysis results (Fig. S2b). We believe that the as-prepared NOMC with high surface area and mesopores is suitable as a support material for designing the advanced electrocatalyst in alkaline HER. Meanwhile, aPt/pNi-NOMC electrocatalyst was prepared by synthesizing the pNi-NOMC first and followed by the atomically dispersed Pt (Fig. S3). The TEM images of the pNi-NOMC confirmed that Ni nanoparticles were homogeneously dispersed into the cylindrical mesoporous structures of the NOMC (Fig. S4). ICP-OES analysis results indicated that the total amount of Ni nanoparticles was 4.64 wt% in pNi-NOMC (Table S1). In the case of aPt/pNi-NOMC, the total amount of Ni nanoparticle was 4.26%, which was controlled almost the same as pNi-NOMC to

thoroughly elucidate the modulation of electrocatalytic activity by different designs of electrocatalysts. To characterize the structures of the aPt/pNi-NOMC electrocatalyst in detail, we performed high angle annular dark field-scanning TEM (HAADF-STEM) and EDS mapping analyses. No big, agglomerated particles were observed in the low-magnification TEM, HAADF-STEM, and EDS mapping images of aPt/pNi-NOMC (Fig. 1b and c), which suggests the following conclusions: i) Ni nanoparticles remained stable without a significant amount of aggregation during the synthetic process to atomically disperse the Pt on the surface of the Ni nanoparticles and ii) Pt was atomically well-dispersed without formation of large nanoparticles. To clearly confirm the atomically dispersed Pt on the surface of the Ni nanoparticles, electron microscopy analyses were performed at higher resolution. The high-resolution STEM and EDS mapping images of aPt/pNi-NOMC indicated that Pt was atomically dispersed on the surface of the Ni nanoparticles supported by NOMC (Fig. 1d and S5). Meanwhile, Pt electrocatalysts which were atomically dispersed in NOMC without any Ni nanoparticles (aPt-NOMC) were also synthesized as a control group to investigate the effect of H^* binding site separation

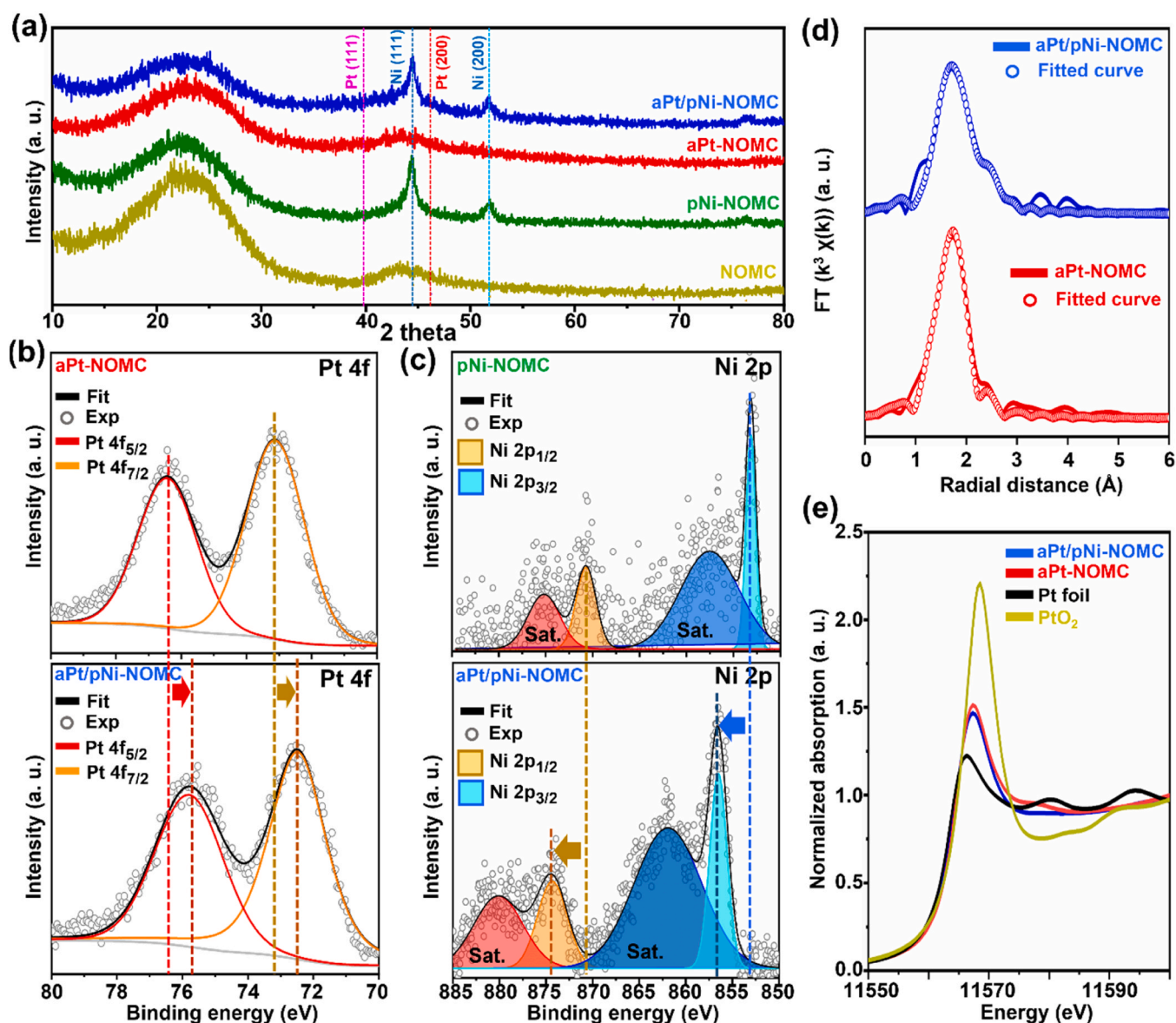


Fig. 2. (a) XRD patterns of NOMC, pNi-NOMC, aPt-NOMC, and aPt/pNi-NOMC. (b) XPS Pt 4f spectra of aPt-NOMC and aPt/pNi-NOMC. (c) XPS Ni 2p spectra of pNi-NOMC and aPt/pNi-NOMC. The overall binding energy of XPS spectra were corrected with reference to C 1s spectra (284.8 eV). (d) k^3 -weighted FT-EXAFS spectra and (e) XANES spectra of aPt-NOMC and aPt/pNi-NOMC at the Pt L_3 edge.

by Ni nanoparticles (see experimental). The total amounts of Pt in aPt-NOMC (4.57 wt%) and aPt/pNi-NOMC (4.53 wt%) were controlled almost the same for a fair comparison (Table S1). The TEM image of the as-prepared aPt-NOMC shows the atomically dispersed Pt on the surface of NOMC (Fig. S6).

XRD analysis was performed to characterize the crystalline structures of each electrocatalyst (Fig. 2a). The XRD patterns of aPt/pNi-NOMC and pNi-NOMC exhibit the two crystalline peaks at 44.5° and 51.8° which correspond to (111) and (200) planes of face-centered cubic phase Ni (JCPDS No.04–0850). Meanwhile, no representative crystalline peaks for Pt are observed in the XRD patterns of aPt/pNi-NOMC and aPt-NOMC, which supports the atomically dispersed Pt, well-matched with the results of electron microscopy analyses. The porous structures of these three electrocatalysts were further investigated. The aPt/pNi-NOMC, pNi-NOMC, and aPt-NOMC reveal similar isotherm linear plots and pore size distribution plots (Fig. S7). The pore sizes of all the electrocatalysts are 5.7 nm, whereas the specific surface areas of aPt/pNi-NOMC, pNi-NOMC, and aPt-NOMC are 935, 952, and $780 \text{ m}^2 \text{ g}^{-1}$, respectively (Table S2). The surface chemical states of the NOMC, aPt/pNi-NOMC, pNi-NOMC, and aPt-NOMC were characterized by XPS analysis. The XPS N 1s spectrum of NOMC show the representative peaks corresponding to several N functionalities including pyridinic and pyrrolic N, which demonstrate the N-doped surface of NOMC (Fig. S8). These N functionalities are favorable for increasing the affinity of a metal precursor onto a NOMC support, which creates homogeneous incorporation of metal nanoparticles on the surface of NOMC [40]. Further, lone-pair electrons of N functionalities inherently enhance the interaction of active polar species in an electrolyte with NOMC support, which thus improves the electrocatalytic activity [53,54]. Meanwhile, the XPS Pt 4f spectra of aPt-NOMC and aPt/pNi-NOMC show two characteristic peaks which correspond to Pt $4f_{5/2}$ and Pt $4f_{7/2}$ (Fig. 2b) [55]. In the case of aPt-NOMC, the Pt $4f_{5/2}$ and Pt $4f_{7/2}$ peaks are positioned at 76.4 and 73.1 eV, respectively [56]. The aPt/pNi-NOMC shows the Pt $4f_{5/2}$ and Pt $4f_{7/2}$ peaks at 75.8 and 72.5 eV, respectively. This negative shift of Pt $4f_{5/2}$ and Pt $4f_{7/2}$ peaks in aPt/pNi-NOMC compared to aPt-NOMC indicates that electrons transfer from Ni nanoparticles to Pt atoms, so the electron density of the Pt increases [57]. In the case of Ni 2p spectra of pNi-NOMC and aPt/pNi-NOMC, four characteristic peaks, namely, Ni $2p_{1/2}$, Ni $2p_{1/2}$ satellite (sat.), Ni $2p_{3/2}$, and Ni $2p_{3/2}$ sat. are observed (Fig. 2c) [58]. In the Ni 2p spectrum of pNi-NOMC, Ni $2p_{1/2}$, Ni $2p_{1/2}$ sat., Ni $2p_{3/2}$, and Ni $2p_{3/2}$ sat. peaks are positioned at 870.7, 875.2, 853.2, and 857.5 eV, respectively, whereas aPt/pNi-NOMC exhibits positively shifted peaks (i.e., Ni $2p_{1/2}$, Ni $2p_{1/2}$ sat., Ni $2p_{3/2}$, and Ni $2p_{3/2}$ sat. at 874.4, 880.2, 856.5, and 861.9 eV, respectively). Compared to the pNi-NOMC, the positive shift of Ni 2p peaks in aPt/pNi-NOMC is attributed to the i) change of valence state of Ni atom (i.e., higher oxidation state) during the Pt SA incorporation process and the ii) electron transfer from the Ni nanoparticles to Pt atoms. The series of electron microscopy and XPS analyses results clearly suggest that Pt is atomically dispersed on the surface of Ni nanoparticles in the aPt/pNi-NOMC electrocatalyst. The local atomic structures and electronic states of the aPt/pNi-NOMC electrocatalyst were further investigated by XAS analysis. The Fourier-transformed extended X-ray absorption fine structure (FT-EXAFS) spectra of the electrocatalysts clearly shows the absence of Pt-Pt bonding near 2.6 \AA [56], suggesting the presence of atomically dispersed Pt in the electrocatalysts (Fig. 2d). To precisely evaluate the local atomic structure of Pt, geometric factors such as coordination atoms and their numbers were determined through EXAFS fitting (Table S3). EXAFS fitting of the aPt-NOMC revealed that Pt forms bonds with both the N or C originating from the NOMC support and the surface Cl ligand derived from the precursor. In contrast, the EXAFS fitting result of aPt/pNi-NOMC distinctly indicates a significant reduction in the Pt-N or C bond, accompanied by the emergence of a new bond with Ni. These results confirm effective control over the local environment of the Pt SA. Furthermore, in the X-ray absorption near edge structure (XANES) spectra of the electrocatalysts, aPt/pNi-NOMC

displayed a slightly reduced white line intensity in comparison to aPt-NOMC (Fig. 2e). The white line represents the electronic transition from the core level to the unoccupied valence state level. A reduction in white line intensity indicates a decrease in vacancies within the valence orbital, suggesting a more reduced electronic structure. This correlation is in line with the observations from XPS analysis.

3.2. Study on HER kinetics and stability of the aPt/pNi-NOMC electrocatalyst

To compare the electrocatalytic activity of aPt/pNi-NOMC, aPt-NOMC, and pNi-NOMC with commercial electrocatalysts, Pt/C and Ni/C electrocatalysts with different amounts of Pt and Ni (i.e., 10, 20, and 40 wt%) were used as a control group (Table S4). The TEM, XRD, and N_2 physisorption analyses were performed to characterize the physical/chemical properties of Pt/C and Ni/C (Fig. S9–11 and Table S5). The electrocatalytic activity of each electrocatalyst was investigated by LSV analysis in H_2 -saturated 1.0 M KOH (Fig. 3a and Table S6). The overpotential required to reach 10 mA cm^{-2} (η_{10}) is 353.8 mV for aPt-NOMC, indicating that Pt SA alone exhibits low activity for an alkaline HER. In contrast, aPt/pNi-NOMC showed a significantly reduced η_{10} value compared to aPt-NOMC (Fig. 3b), approaching the value of 40 wt % Pt/C while using only 1/8.72 of the Pt areal loading. Furthermore, the overpotential at 50 mA cm^{-2} (η_{50}) and 100 mA cm^{-2} (η_{100}) of aPt/pNi-NOMC is 142.2 and 199.1 mV, respectively, which is similar or even lower than those of 40 wt% Pt/C (141.4 and 226.0 mV for η_{50} and η_{100} , respectively) (Fig. S12a and b). Ni/C electrocatalysts with various Ni amounts also show much higher overpotential than aPt/pNi-NOMC at 10 mA cm^{-2} and 50 mA cm^{-2} (Fig. S13), and therefore the synergistic effect between Pt SA and Ni could contribute to the kinetic enhancement of the alkaline HER. It is noteworthy that the aPt/pNi-NOMC electrocatalyst with an areal Pt loading amount of $9.03 \mu\text{gPt cm}^{-2}$ and an areal Ni loading amount of $8.49 \mu\text{gNi cm}^{-2}$ exhibits a lower overpotential than commercial Pt/C and Ni/C electrocatalysts with much higher areal loading amounts of Pt (19.14, 40.27, and $78.74 \mu\text{gPt cm}^{-2}$ for 10, 20, and 40 wt% Pt/C, respectively) and Ni (21.53, 42.86, and $83.52 \mu\text{gNi cm}^{-2}$ for 10, 20, and 40 wt% Ni/C, respectively) (Table S6). Meanwhile, mass activity is an important indicator in estimating the cost efficiency and atomic economy of electrocatalysts [59,60]. The mass activity of aPt/pNi-NOMC is $11.13 \text{ A mgPt}^{-1}$ at -0.2 V (vs. RHE) which is 29, 8, 7, and 11 times that of aPt-NOMC (0.39 A mgPt^{-1}), 10 wt% Pt/C (1.40 A mgPt^{-1}), 20 wt% Pt/C (1.69 A mgPt^{-1}), and 40 wt% Pt/C (1.06 A mgPt^{-1}), respectively (Fig. 3c and d). Further, ECSA of each electrocatalyst was estimated using CV analysis at a scan rate of 50 mV s^{-1} based on the desorption of H_{upd} (Fig. S14 and Table S7). The specific activity (i.e., maximum current density per ECSA) of each electrocatalyst was evaluated by normalizing current densities by ECSA (Fig. S15). The specific activity of aPt/pNi-NOMC is much higher than that of aPt-NOMC, 10, 20, and 40 wt% Pt/C. In addition, the Tafel slope and EIS measurement were evaluated to further investigate the HER kinetics of the aPt/pNi-NOMC electrocatalyst. The Tafel slope of aPt/pNi-NOMC is 40 mV dec^{-1} which implies that Heyrovsky step (i.e., evolution of H_2 from the H^* adsorbed on electrocatalyst surface and hydrogen in water molecule) is a RDS of alkaline HER for aPt/pNi-NOMC [61,62]. On the other hand, 10 wt% Pt/C exhibits a Tafel slope of 84 mV dec^{-1} , much higher than that of aPt/pNi-NOMC. It suggests that alkaline HER kinetic was highly enhanced by aPt/pNi-NOMC electrocatalyst (Fig. 3e). In the results of EIS analysis at -0.1 V (vs. RHE), the Nyquist plot of aPt/pNi-NOMC has a smaller semicircle size than that of 10 wt% Pt/C (Fig. 3f). Considering that a semicircle size of the Nyquist plot at a high-to-medium frequency region corresponds to the charge transfer resistance [60], the aPt/pNi-NOMC electrocatalyst is more favorable for facilitating the transfer of charge with surface adsorbed reaction intermediates and increasing the reaction rate than 10 wt% Pt/C.

Apart from reaction kinetics, stability of the electrocatalyst in an

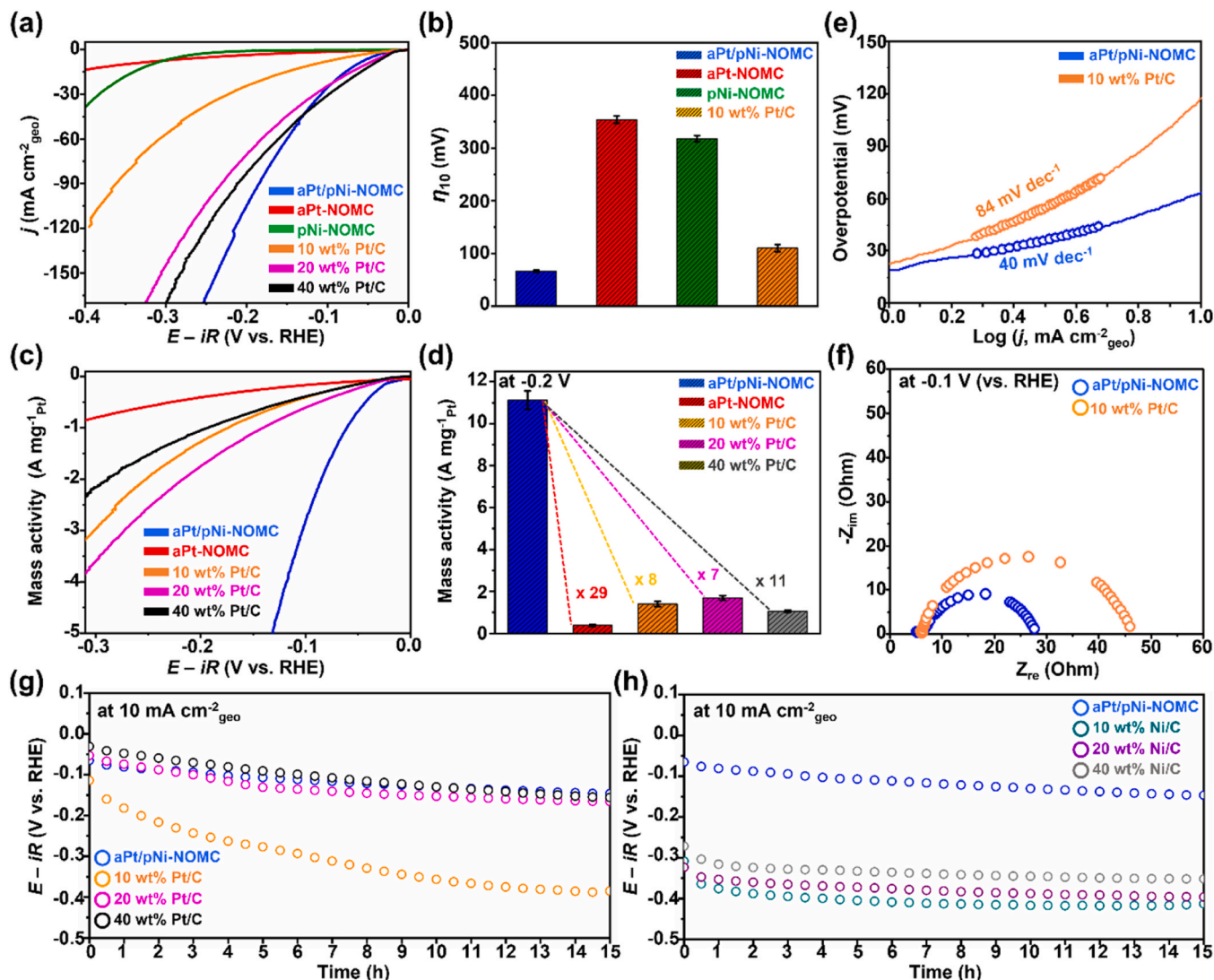


Fig. 3. (a) LSV curves of each electrocatalyst measured in a H₂-saturated 1.0 M KOH electrolyte with a potential scan rate of 5 mV s⁻¹. (b) Summarized η_{10} values of aPt/pNi-NOMC, aPt-NOMC, pNi-NOMC, and 10 wt% Pt/C. (c) Mass activity polarization curves and (d) the summarized mass activity of aPt/pNi-NOMC, aPt-NOMC, and Pt/C with different amounts of Pt at -0.2 V (vs. RHE). Error bars are the standard deviation of five experiments. (e) Tafel slopes and (f) Nyquist plots of aPt/pNi-NOMC and 10 wt% Pt/C. EIS analysis was performed at -0.1 V (vs. RHE). Comparison of the electrocatalyst stability of aPt/pNi-NOMC with (g) Pt/C with different amounts of Pt and (h) Ni/C with different amounts of Ni at a current density of 10 mA cm⁻².

alkaline electrolyte is also a pivotal parameter in realizing the practical alkaline HER. Thus, the stability of each electrocatalyst was characterized by chronopotentiometry analysis at a current density of 10 mA cm⁻² for 15 h in H₂-saturated 1.0 M KOH (Fig. 3g and h). For the 10 wt% Pt/C, a substantial increase in overpotential was observed after 15 h (Fig. 3g). In contrast, when compared to the 10 wt% Pt/C, the aPt/pNi-NOMC electrocatalyst demonstrated a sustained and relatively stable potential over the same 15 h. Particularly noteworthy is the fact that the marginal potential change observed in the aPt/pNi-NOMC electrocatalyst is comparable to that of 20 and 40 wt% Pt/C electrocatalysts. In contrast, the observed potential alteration in the aPt/pNi-NOMC electrocatalyst is notably smaller compared to the variations observed in the cases of 10, 20, and 40 wt% of Ni/C electrocatalysts (Fig. 3h). In addition to the chronopotentiometry analysis, ADT with CV analysis for 1000 cycles was performed in H₂-saturated 1.0 M KOH at a scan rate of 100 mV s⁻¹ to explore the long-term stability of each electrocatalysts (Fig. 4a). After ADT, the 10, 20, and 40 wt% Pt/C electrocatalysts exhibit the η_{50} of 291.1, 281.6, and 217.3 mV, respectively, whereas the η_{50} of aPt/pNi-NOMC electrocatalyst is 168.2 mV (i.e., the lowest among the four electrocatalysts) (Fig. 4b). Similarly, the η_{100} of aPt/pNi-NOMC

electrocatalyst (227.5 mV) is also much lower than other Pt/C electrocatalysts (355.6, 352.0, and 315.2 mV for 10, 20, and 40 wt% Pt/C, respectively) (Fig. S16). More importantly, the change of η_{50} and η_{100} values before and after ADT (i.e., $\Delta\eta_{50}$ and $\Delta\eta_{100}$) is only 26.0 and 28.4 mV, respectively for aPt/pNi-NOMC. On the other hand, the $\Delta\eta_{50}$ of 20 and 40 wt% Pt/C electrocatalysts is 116.4 and 75.9 mV, respectively, and $\Delta\eta_{100}$ of 20 and 40 wt% Pt/C electrocatalysts is 101.2 and 89.2 mV, respectively, which is much higher than those of aPt/pNi-NOMC electrocatalyst. Even compared to 10, 20, and 40 wt% Ni/C electrocatalysts, the aPt/pNi-NOMC electrocatalyst exhibits the lowest overpotential after ADT (Fig. S17). Moreover, the mass activity of aPt/pNi-NOMC, which was estimated at -0.2 V (vs. RHE) after ADT, is 8.27 A mg_{Pt}⁻¹ which is 10, 14, and 15 times higher than 10, 20, and 40 wt% Pt/C electrocatalysts, respectively (Fig. 4c). Meanwhile, the HAADF-STEM and EDS mapping images of aPt/pNi-NOMC after ADT show that i) Ni nanoparticles are homogeneously distributed without severe agglomeration and ii) Pt is atomically well-dispersed in aPt/pNi-NOMC electrocatalyst even after CV cycling for 1000 cycles (Fig. 4d). On the other hand, HAADF-STEM and EDS mapping images of 10 wt% Pt/C before and after ADT show partially agglomerated Pt nanoparticles during

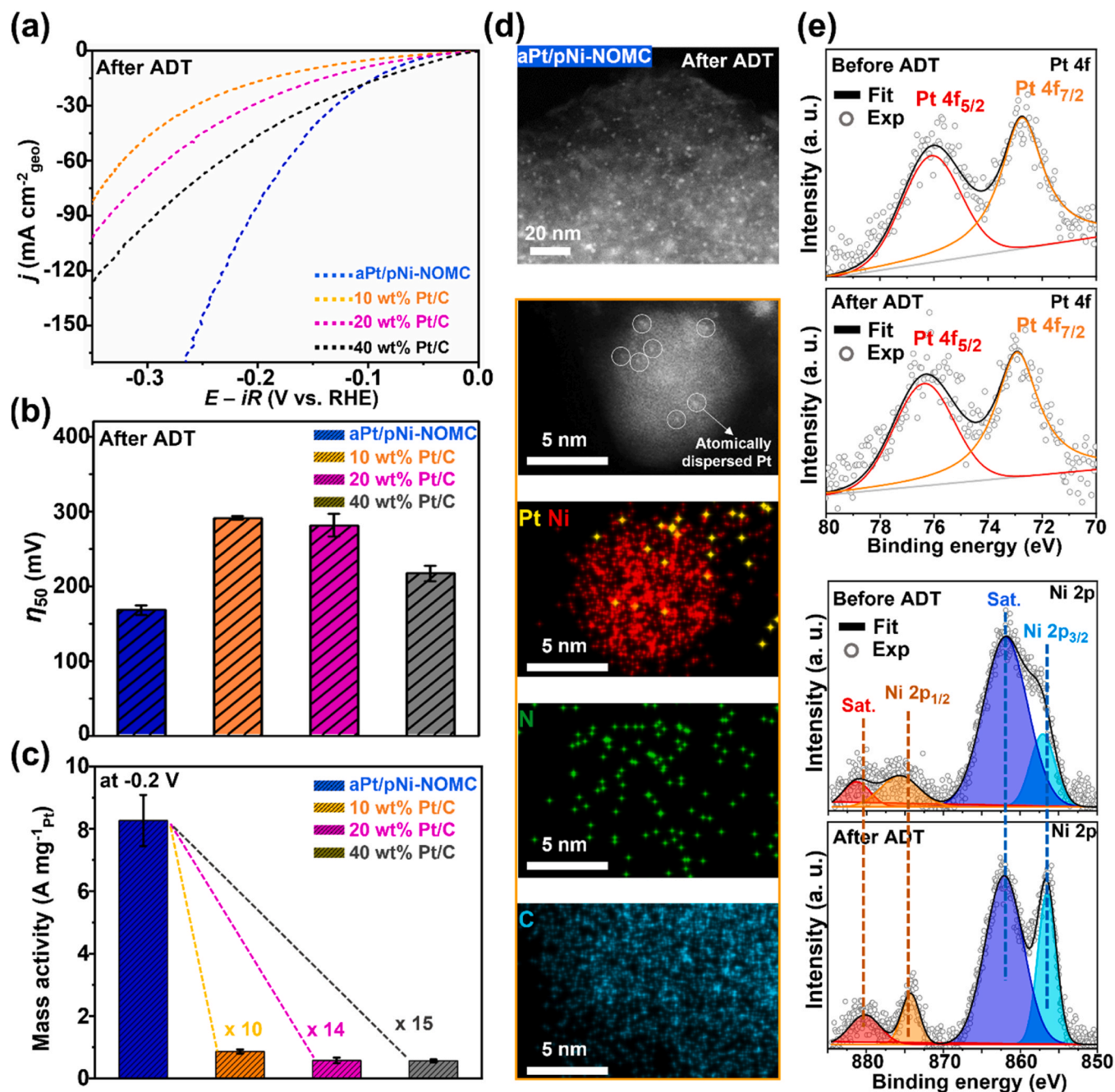


Fig. 4. (a) LSV curves, (b) summarized η_{50} values, and (c) summarized mass activity values of aPt/pNi-NOMC and Pt/C with different amounts of Pt after ADT. Error bars are the standard deviation of five experiments. (d) Ex-situ HAADF-STEM and EDS mapping images of aPt/pNi-NOMC after ADT. (e) Ex-situ XPS Pt 4f and Ni 2p spectra of aPt/pNi-NOMC after ADT.

repetitive ADT (Fig. S18). The XPS Pt 4f and Ni 2p spectra of aPt/pNi-NOMC electrocatalyst-embedded electrode show the ignorable changes before and after the ADT (Fig. 4e). Compared to XPS Ni 2p spectrum of aPt/pNi-NOMC electrocatalyst powder (suggested in Fig. 2c), the relative decrease in Ni 2p_{3/2} peak intensity of aPt/pNi-NOMC-embedded electrode is attributed to the presence of Nafion in electrode which can be related with the strong Ni-F bonding at ~ 860.7 eV [63]. Meanwhile, Pt 4f spectra of 10 wt% Pt/C electrocatalyst-embedded electrode exhibit the negative shift of Pt 4f_{5/2} and Pt 4f_{7/2} peaks after ADT due to the severe agglomeration of Pt species (Fig. S19) [64]. In contrast, the N functionalities-containing NOMC support prevents the agglomeration of Ni nanoparticles and moreover strong binding between Pt-Ni with electron transfer help the

presence of atomically dispersed Pt, which is consistent with the microscopic analysis result. Consequently, these electrochemical stability test and ex-situ material characterization results corroborate that aPt/pNi-NOMC electrocatalyst has high long-term stability for the HER in alkaline media.

3.3. Origin of enhanced HER kinetics with an aPt/pNi-NOMC electrocatalyst

To elucidate the origin of the enhanced HER kinetics of this specially designed aPt/pNi-NOMC electrocatalyst, the alkaline HER mechanism was investigated by DFT calculations using three different slab models: aPt/pNi, aPt-NOMC, and pNi surfaces. Details of the models are

summarized in the *Computational details* section. Fig. 5a and b shows the Gibbs free energy diagrams and optimized structures for all the elementary reaction steps involved in the alkaline HER on each surface. The first two key steps in the alkaline HER are the adsorption and dissociation of water (Volmer step), followed by the desorption of H_2 (Heyrovsky step or Tafel step). As shown in Fig. 5a and S20, we found that water can spontaneously adsorb on the aPt/pNi and aPt-NOMC surfaces with adsorption free energies of -0.39 and -0.81 eV, respectively, forming a chemical bond between the Pt SA and the O atom of the water molecule, while water adsorption on the pNi is energetically less favorable with an adsorption free energy of 0.01 eV. In general, strong adsorption of water is advantageous for water dissociation and indeed, as depicted in Fig. 5c-e and S21, the free energy barriers for breaking the H–OH bond of water are lower on the aPt/pNi and aPt-NOMC surfaces (0.12 and 0.21 eV, respectively) than on the pNi surface (0.62 eV). The kinetic barrier for water dissociation from the pNi surface is in good agreement with the value reported by Richards et al. (0.69 eV) [65], and is much higher than the reaction free energies of the other elementary reaction steps in HER, indicating that the Volmer step is the rate-determining step (RDS) for pNi. Conversely, when Pt SA is incorporated on pNi, as in aPt/pNi, the kinetic barrier for water dissociation decreases significantly from 0.62 to 0.12 eV. This may be due to the fact that the H^* and OH^* formed by breaking the strong H–OH bond of water are stabilized separately on the Ni atom and the Pt SA on the surface, respectively. For the aPt/pNi surface, the subsequent H_2 desorption step requiring a free energy of 0.33 eV becomes RDS due to the accelerated Volmer step, which is well-matched with Tafel slope results. In addition to the kinetics for water dissociation and the desorption of H_2 , the adsorption of OH^* on the surfaces is another critical factor to consider when evaluating HER activity in alkaline media. It is important that the adsorption of OH^* is not overly strong or weak, as strong OH^* adsorption can be beneficial for water dissociation but can also hinder the desorption of OH^* from the surface and thus block the active site of the HER. Among the three examined surfaces, the aPt/pNi and pNi surfaces exhibit relatively appropriate OH^* adsorption free energies of -3.13 and -2.98 eV, respectively (Fig. S22). In contrast,

the aPt-NOMC surface displays a highly negative OH^* adsorption free energy of -4.08 eV, which prevents the surface of the electrocatalyst from returning to its original state. Consequently, for aPt-NOMC, unlike for the other surfaces, the final reaction step of OH^* requires a higher free energy of 1.02 eV than the other steps, resulting in this step being the RDS. To summarize, the free energy change for RDS (ΔG_{RDS}) becomes higher in the order of aPt/pNi (0.33 eV), pNi (0.62 eV), and aPt-NOMC (1.02 eV). This demonstrates that the enhanced HER kinetics of the aPt/pNi-NOMC electrocatalyst is mainly due to the synergistic effect between Pt SA and pNi, which provides atomically separated adsorption sites for H^* and OH^* to efficiently promote the water dissociation as well as properly balanced OH^* adsorption.

3.4. Fabrication and test of AEMWE single cell

To investigate the practical feasibility of the aPt/pNi-NOMC electrocatalyst for a high-performance alkaline HER, an AEMWE single cell was assembled and tested using aPt/pNi-NOMC, $\text{Co}_3\text{O}_4/\text{NF}$, X37–50, and NF as the cathode electrocatalyst, anode electrocatalyst, AEM, and PTL, respectively. Furthermore, for comparison with commercial Pt-based electrocatalysts for HER, an AEMWE single cell equipped with a 10 and 40 wt% Pt/C electrocatalyst as the cathode was prepared (Fig. 6a and S25). The LSV curve of the AEMWE single cell with the aPt/pNi-NOMC electrocatalyst tested in 1.0 M KOH at 45°C reached a current density of 0.79 A cm^{-2} at 1.9 V_{cell} (V_{cell}: total cell voltage), exhibiting higher performance than that of the 10 and 40 wt% Pt/C electrocatalyst-embedded AEMWE single cell (0.43 A and 0.31 A cm^{-2} at 1.9 V_{cell}, respectively) (Fig. 6b and S26). Even at high temperature conditions (*i.e.*, 60 and 75°C), the aPt/pNi-NOMC electrocatalyst exhibits higher cell performance compared to the 10 and 40 wt% Pt/C (Fig. 6c, S27, and S28). The aPt/pNi-NOMC electrocatalyst achieved current densities of 0.96 A cm^{-2} at 1.9 V_{cell} for 60°C and 1.14 A cm^{-2} for 75°C , while the 10 and 40 wt% Pt/C reached current densities of 0.74 and 0.41 A cm^{-2} for 60°C , and 0.99 and 0.46 A cm^{-2} for 75°C , respectively, showing an improved cell performance as the operating temperature increases. The current density of the aPt/pNi-NOMC electrocatalyst measured at

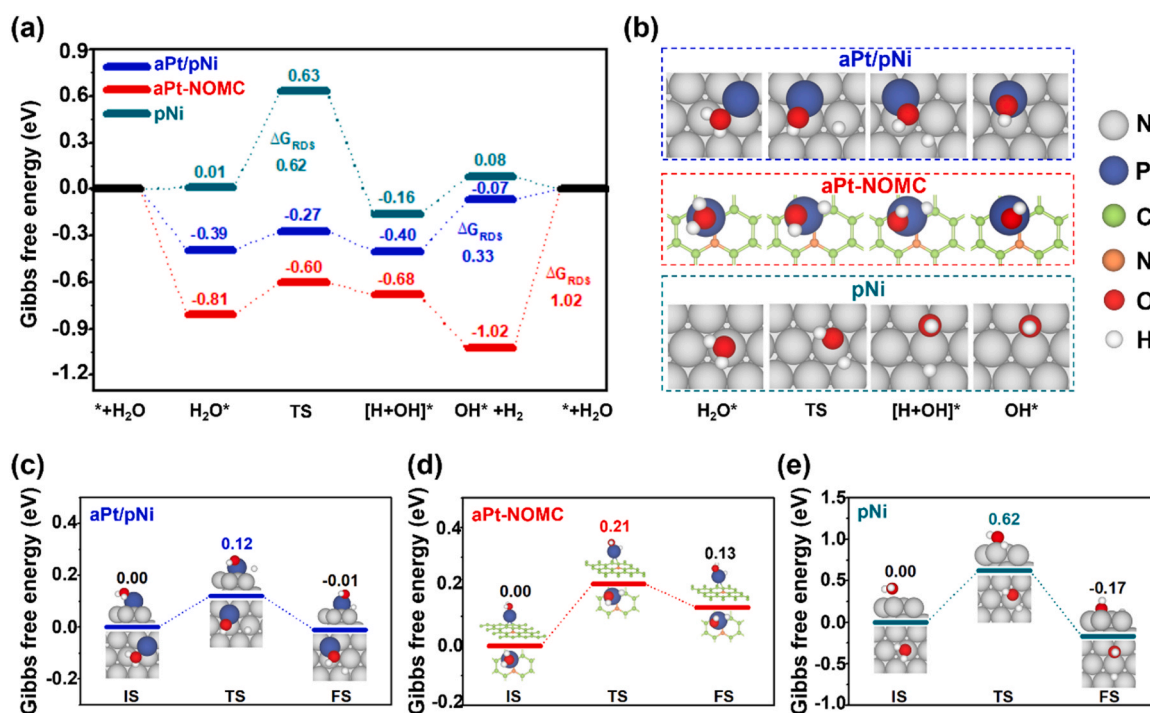


Fig. 5. (a) Gibbs free energy diagrams and (b) optimized structures of reaction intermediates involved in alkaline HER on aPt/pNi (blue), aPt-NOMC (red), and pNi (green) surfaces. Gibbs free energy barriers for water dissociation on (c) aPt/pNi, (d) aPt-NOMC, and (e) pNi surfaces.

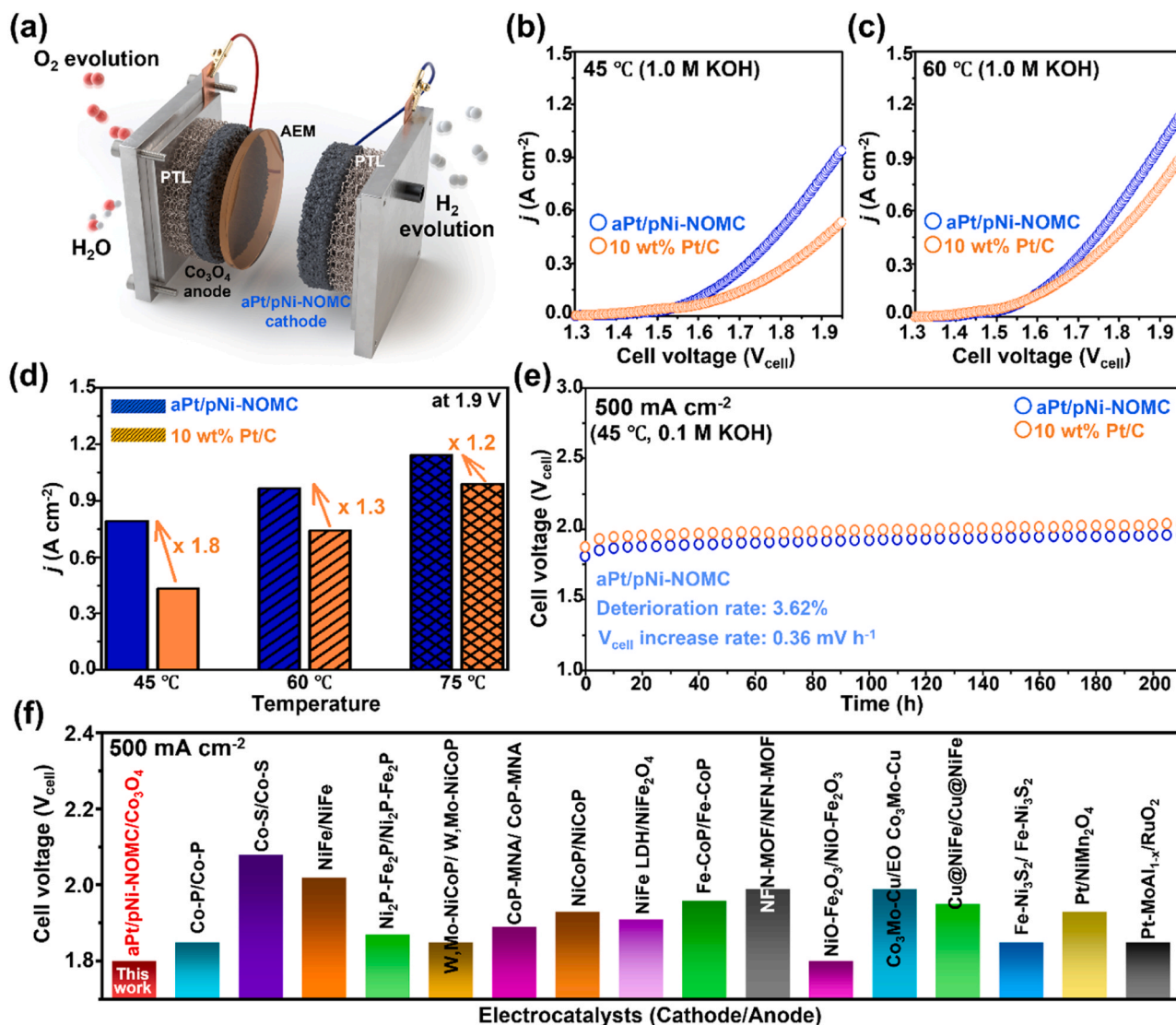


Fig. 6. Electrochemical test results of AEMWE single cell. (a) Schematics of an AEMWE single cell. LSV curves of aPt/pNi-NOMC and 10 wt% Pt/C in a 1.0 M KOH electrolyte at (b) 45 and (c) 60 °C at a scan rate of 1 mV s⁻¹. (d) Summarized current densities of aPt/pNi-NOMC and 10 wt% Pt/C evaluated with a 1.9 V of cell voltage with the different operating temperatures. (e) Durability test of aPt/pNi-NOMC and 10 wt% Pt/C at 45 °C and a current density of 500 mA cm⁻² using a 0.1 M KOH electrolyte. (f) Comparison of V_{cell} values of the AEMWE cell with previously reported state-of-the-art electrocatalysts.

1.9 V_{cell} is 1.8, 1.3, and 1.2 times higher than that of 10 wt% Pt/C at 45, 60, and 75 °C, respectively. It also exhibits 2.6, 2.4, and 2.5 times higher current density than the 40 wt% Pt/C electrocatalyst at the same temperatures (Fig. 6d and S29). In this observation, it is evident that the aPt/pNi-NOMC cathode exhibits lower sensitivity to cell temperature compared to the Pt/C cathode. This suggests that the apparent activation energy (E_a) of the HER on aPt/pNi-NOMC is smaller than that on Pt/C, suggesting the accelerated HER kinetics by the aPt/pNi-NOMC electrocatalyst [66]. Moreover, the durability of AEMWE single cells with aPt/pNi-NOMC and 10 wt% Pt/C electrocatalysts applied was also evaluated at the 45 °C with the constant current density of 500 mA cm⁻² (Fig. 6e). For this durability test, a 0.1 M KOH electrolyte was used to suppress the deterioration of the membrane. In the case of the 10 wt% Pt/C electrocatalyst, the deterioration rate is 3.89% for 210 h, indicating that the rate of potential increase per hour is 0.42 mV h⁻¹. On the other hand, the aPt/pNi-NOMC electrocatalyst shows a deterioration rate of 3.62% and the rate of potential increase per hour of 0.36 mV h⁻¹, which suggests that the aPt/pNi-NOMC electrocatalyst is more favorable than the 10 wt% Pt/C electrocatalyst for improving the practical durability of the AEMWE single cell. Consequently, atomically separating the H*

binding site in the specially-designed aPt/pNi-NOMC electrocatalyst is efficient in enhancing the kinetics of the alkaline HER at the AEMWE single cell level by facilitating the water dissociation step and simultaneously optimizing the HBE and OHBE. It is noteworthy that the V_{cell} of the AEMWE single cell achieved by the aPt/pNi-NOMC electrocatalyst at a high current density of 500 mA cm⁻² is outstanding, compared with previously reported V_{cell} values of the AEMWE (Fig. 6f and Table S8). Therefore, we believe that the strategy of atomically separating the H* binding site of SA-based electrocatalysts using adjacent metal nanoparticles will shine light on the development of advanced electrocatalysts for high-performance alkaline HERs.

4. Conclusion

In summary, we proposed that the introduction of Ni nanoparticle artificial ensemble sites adjacent to the Pt SA can induce the atomical separation of H* and OH* binding sites. The separated binding of H* on Ni atoms and OH* on Pt SA highly improves the alkaline HER kinetics by accelerating the dissociation of strong OH–H bonding of water molecules in the Volmer step and optimizing the HBE and OHBE for favorable

adsorption-desorption behaviors of active species. Further, NOMC with a high surface area and a cylindrical mesoporous structure was used as a support material for designing the alkaline HER electrocatalyst to maximize its electrocatalytic activity. Consequently, this advanced aPt/pNi-NOMC electrocatalyst with 4.53 wt% of Pt (areal Pt loading of $9.03 \mu\text{g}_{\text{Pt}} \text{cm}_{\text{geo}}^{-2}$) showed similar or even lower overpotentials at $50 \text{ mA cm}_{\text{geo}}^{-2}$ and $100 \text{ mA cm}_{\text{geo}}^{-2}$ than Pt/C electrocatalysts with 40 wt% of Pt (areal loading of $78.74 \mu\text{g}_{\text{Pt}} \text{cm}_{\text{geo}}^{-2}$) in the half cell. More importantly, a high-performance AEMWE single cell with $1.8 \text{ V}_{\text{cell}}$ at 500 mA cm^{-2} and a V_{cell} increase rate of only 0.36 mV h^{-1} over 210 h was achieved by using aPt/pNi-NOMC as a cathode electrocatalyst. Therefore, we believe that this strategy of separating the H^* and OH^* binding sites by an artificial ensemble site is one of the promising future directions to realize a high-performance practical AEMWE.

CRediT authorship contribution statement

Won-Gwang Lim: Conceptualization, Methodology, Validation, Formal analysis, Investigation, Data curation, Writing – original draft, Writing – review & editing, Visualization. **Hoang Nam Truong:** Conceptualization, Methodology, Validation, Formal analysis, Investigation, Data curation, Writing – original draft, Writing – review & editing, Visualization. **Jae-Yeop Jeong:** Conceptualization, Methodology, Validation, Formal analysis, Investigation, Data curation, Writing – original draft, Writing – review & editing, Visualization. **Dongkyu Kim:** Methodology, Validation, Formal analysis, Investigation, Data curation. **Lee Seul Oh:** Validation, Formal analysis, Investigation, Data curation. **Changshin Jo:** Validation, Discussion, Investigation, Data curation. **Chiho Kim:** Validation, Formal analysis, Investigation, Data curation. **Hyung Ju Kim:** Discussion, Investigation, Data curation, Funding acquisition. **Sung Mook Choi:** Conceptualization, Methodology, Resources, Supervision, Validation, Formal analysis, Investigation, Data curation, Writing-review & editing, Visualization. **Hyeyoung Shin:** Software, Resources, Supervision, Funding acquisition, Validation, Formal analysis, Investigation, Data curation, Writing-review & editing, Visualization. **Seonggyu Lee:** Conceptualization, Methodology, Resources, Supervision, Validation, Formal analysis, Investigation, Data curation, Writing-review & editing, Visualization. **Eunho Lim:** Conceptualization, Methodology, Resources, Supervision, Funding acquisition, Validation, Formal analysis, Investigation, Data curation, Writing-review & editing, Visualization, Project administration.

Declaration of Competing Interest

The authors declare that they have no known competing financial interests or personal relationships that could have appeared to influence the work reported in this paper.

Data Availability

Data will be made available on request.

Acknowledgement

This research was supported by the KRICT project (No. KK2311-30) from the Korea Research Institute of Chemical Technology (KRICT). This research was supported by the Ministry of Trade, Industry, and Energy (MOTIE), Korea, under “Innovative Digital Manufacturing Platform” (No. P0022331) supervised by the Korea Institute for Advancement of Technology (KIAT). This work was supported by the National Research Foundation of Korea (NRF) grant funded by the Korea government (MSIT) (No. NRF-2021R1A5A1084921).

Appendix A. Supporting information

Supplementary data associated with this article can be found in the

online version at doi:10.1016/j.apcatb.2023.123568.

References

- [1] S. Lee, M. Ashwin Kishore, D. Kim, H. Kang, J. Chun, L.S. Oh, J.H. Park, H.J. Kim, J.S. Yoo, E. Lim, Direct O–O coupling promoted the oxygen evolution reaction by dual active sites from Ag/LaNiO₃ interfaces, *ACS Appl. Energy Mater.* 5 (2022) 14658–14668.
- [2] T.P. Vispute, G.W. Huber, Production of hydrogen, alkanes and polyols by aqueous phase processing of wood-derived pyrolysis oils, *Green. Chem.* 11 (2009) 1433–1445.
- [3] C. Liu, J. Qian, Y. Ye, H. Zhou, C.-J. Sun, C. Sheehan, Z. Zhang, G. Wan, Y.-S. Liu, J. Guo, Oxygen evolution reaction over catalytic single-site Co in a well-defined brookite TiO₂ nanorod surface, *Nat. Catal.* 4 (2021) 36–45.
- [4] Y.S. Park, J. Yang, J. Lee, M.J. Jang, J. Jeong, W.-S. Choi, Y. Kim, Y. Yin, M.H. Seo, Z. Chen, Superior performance of anion exchange membrane water electrolyzer: Ensemble of producing oxygen vacancies and controlling mass transfer resistance, *Appl. Catal. B: Environ.* 278 (2020), 119276.
- [5] D. Kim, L.S. Oh, J.H. Park, H.J. Kim, S. Lee, E. Lim, Perovskite-based electrocatalysts for oxygen evolution reaction in alkaline media: A mini review, *Front. Chem.* 10 (2022), 1024865.
- [6] J.Q. Chi, X.J. Zeng, X. Shang, B. Dong, Y.M. Chai, C.G. Liu, M. Marin, Y. Yin, Embedding RhPx in N, P co-doped carbon nanoshells through synergetic phosphorization and pyrolysis for efficient hydrogen evolution, *Adv. Funct. Mater.* 29 (2019) 1901790.
- [7] Y. Dong, Z. Deng, Z. Xu, G. Liu, X. Wang, Synergistic Tuning of CoO/CoP heterojunction nanowire arrays as efficient bifunctional catalysts for alkaline overall water splitting, *Small Methods* 7 (2023) 2300071.
- [8] F. Safizadeh, E. Ghali, G. Houlachi, Electrocatalysis developments for hydrogen evolution reaction in alkaline solutions—a review, *Int. J. Hydrog.* 40 (2015) 256–274.
- [9] Y. Zheng, Y. Jiao, A. Vasileff, S.Z. Qiao, The hydrogen evolution reaction in alkaline solution: from theory, single crystal models, to practical electrocatalysts, *Angew. Chem. Int. Ed.* 57 (2018) 7568–7579.
- [10] N. Mahmood, Y. Yao, J.W. Zhang, L. Pan, X. Zhang, J.J. Zou, Electrocatalysts for hydrogen evolution in alkaline electrolytes: mechanisms, challenges, and prospective solutions, *Adv. Sci.* 5 (2018) 1700464.
- [11] Y. Zhao, J. Hwang, M.T. Tang, H. Chun, X. Wang, H. Zhao, K. Chan, B. Han, P. Gao, H. Li, Ultrastable molybdenum disulfide-based electrocatalyst for hydrogen evolution in acidic media, *J. Power Sources* 456 (2020), 227998.
- [12] M. Lao, P. Li, Y. Jiang, H. Pan, S.X. Dou, W. Sun, From fundamentals and theories to heterostructured electrocatalyst design: An in-depth understanding of alkaline hydrogen evolution reaction, *Nano Energy* 98 (2022), 107231.
- [13] D. Lee, L.S. Oh, H.W. Kim, Y. Kim, W. Yoon, E. Lim, W.B. Kim, J.H. Kim, J.H. Kim, Revealing improved electrocatalytic performances of electrochemically synthesized S and Ni doped Fe₂O₃ nanostructure interfaces, *Appl. Surf. Sci.* 588 (2022), 152894.
- [14] A. Bazan-Aguilar, G. García, E. Pastor, J.L. Rodríguez, A.M. Baena-Moncada, In-situ spectroelectrochemical study of highly active Ni-based foam electrocatalysts for hydrogen evolution reaction, *Appl. Catal. B: Environ.* 336 (2023), 122930.
- [15] N. Danilovic, R. Subbaraman, D. Strmcnik, K.C. Chang, A. Paulikas, V. Stamenkovic, N.M. Markovic, Enhancing the alkaline hydrogen evolution reaction activity through the bifunctionality of Ni(OH)₂/metal catalysts, *Angew. Chem.* 124 (2012) 12663–12666.
- [16] T. Schmidt, P. Ross Jr, N. Markovic, Temperature dependent surface electrochemistry on Pt single crystals in alkaline electrolytes: Part 2. The hydrogen evolution/oxidation reaction, *J. Energy Chem.* 524 (2002) 252–260.
- [17] Y. Wang, L. Li, L. Hu, L. Zhuang, J. Lu, B. Xu, A feasibility analysis for alkaline membrane direct methanol fuel cell: thermodynamic disadvantages versus kinetic advantages, *Electrochem. Commun.* 5 (2003) 662–666.
- [18] H.C. Fu, X.H. Chen, B. Yang, Y.H. Luo, T. Li, X.H. Wang, Q. Zhang, X.L. Li, N.B. Li, H.Q. Luo, Unveiling the in-situ hydrogen intercalation in Mo₂CO_x for promoting the alkaline hydrogen evolution reaction, *Appl. Catal. B: Environ.* 332 (2023), 122739.
- [19] L. Huo, C. Jin, J. Tang, X. Xu, K. Jiang, L. Shang, Y. Li, J. Zhang, L. Zhu, J. Chu, Ultrathin NiPt single-atom alloy for synergistically accelerating alkaline hydrogen evolution, *ACS Appl. Energy Mater.* 5 (2022) 15136–15145.
- [20] S. Zhu, M. Shao, Electrolyte pH-dependent hydrogen binding energies and coverages on platinum, iridium, rhodium, and ruthenium surfaces, *Catal. Sci. Technol.* 12 (2022) 3228–3233.
- [21] Z. Liu, J. Qi, M. Liu, S. Zhang, Q. Fan, H. Liu, K. Liu, H. Zheng, Y. Yin, C. Gao, Aqueous synthesis of ultrathin platinum/non-noble metal alloy nanowires for enhanced hydrogen evolution activity, *Angew. Chem. Int. Ed.* 57 (2018) 11678–11682.
- [22] A. Mosallanezhad, C. Wei, P.A. Koudakan, Y. Fang, S. Niu, Z. Bian, B. Liu, T. Huang, H. Pan, G. Wang, Interfacial synergies between single-atomic Pt and CoS for enhancing hydrogen evolution reaction catalysis, *Appl. Catal. B: Environ.* 315 (2022), 121534.
- [23] Y. Da, Z. Tian, R. Jiang, G. Chen, Y. Liu, Y. Xiao, J. Zhang, S. Xi, W. Chen, X. Han, Single-Atom Pt Doping Induced p-Type to n-Type Transition in NiO Nanosheets toward Self-Gating Modulated Electrocatalytic Hydrogen Evolution Reaction, *ACS Nano* 17 (2023) 18539–18547.
- [24] W. Sheng, M. Myint, J.G. Chen, Y. Yan, Correlating the hydrogen evolution reaction activity in alkaline electrolytes with the hydrogen binding energy on monometallic surfaces, *Energy Environ. Sci.* 6 (2013) 1509–1512.

- [25] Y. Pan, X. Wang, W. Zhang, L. Tang, Z. Mu, C. Liu, B. Tian, M. Fei, Y. Sun, H. Su, Boosting the performance of single-atom catalysts via external electric field polarization, *Nat. Commun.* 13 (2022) 3063.
- [26] X. Yang, Y. Zeng, W. Alnoush, Y. Hou, D. Higgins, G. Wu, Tuning two-electron oxygen-reduction pathways for H₂O₂ electrosynthesis via engineering atomically dispersed single metal site catalysts, *Adv. Mater.* 34 (2022) 2107954.
- [27] Z. Chen, X. Li, J. Zhao, S. Zhang, J. Wang, H. Zhang, J. Zhang, Q. Dong, W. Zhang, W. Hu, Stabilizing Pt single atoms through Pt–Se electron bridges on vacancy-enriched nickel selenide for efficient electrocatalytic hydrogen evolution, *Angew. Chem. Int. Ed.* 62 (2023), e202308686.
- [28] Y. Da, Z. Tian, R. Jiang, Y. Liu, X. Lian, S. Xi, Y. Shi, Y. Wang, H. Lu, B. Cui, Dual Pt–Ni atoms dispersed on N-doped carbon nanostructure with novel (NiPt)–N₄C₂ configurations for synergistic electrocatalytic hydrogen evolution reaction, *Sci. China Mater.* 66 (2023) 1389–1397.
- [29] L. Zou, Y.S. Wei, C.C. Hou, C. Li, Q. Xu, Single-atom catalysts derived from metal–organic frameworks for electrochemical applications, *Small* 17 (2021) 2004809.
- [30] A. Wang, J. Li, T. Zhang, Heterogeneous single-atom catalysis, *Nat. Rev. Chem.* 2 (2018) 65–81.
- [31] B. Wang, X. Zhu, X. Pei, W. Liu, Y. Leng, X. Yu, C. Wang, L. Hu, Q. Su, C. Wu, Room-temperature laser planting of high-loading single-atom catalysts for high-efficiency electrocatalytic, *Hydrog. Evol., J. Am. Chem. Soc.* 145 (2023) 13788.
- [32] N. Wang, R. Mei, X. Lin, L. Chen, T. Yang, Q. Liu, Z. Chen, Cascade anchoring strategy for fabricating high-loading Pt single atoms as bifunctional catalysts for electrocatalytic hydrogen evolution and oxygen reduction reactions, *ACS Appl. Mater. Interfaces* 15 (2023) 29195.
- [33] T. Zhang, J. Jin, J. Chen, Y. Fang, X. Han, J. Chen, Y. Li, Y. Wang, J. Liu, L. Wang, Pinpointing the axial ligand effect on platinum single-atom-catalyst towards efficient alkaline hydrogen evolution reaction, *Nat. Commun.* 13 (2022) 6875.
- [34] Y. Zheng, Y. Jiao, Y. Zhu, L.H. Li, Y. Han, Y. Chen, M. Jaroniec, S.-Z. Qiao, High electrocatalytic hydrogen evolution activity of an anomalous ruthenium catalyst, *J. Am. Chem. Soc.* 138 (2016) 16174–16181.
- [35] R. Wan, M. Luo, J. Wen, S. Liu, X. Kang, Y. Tian, Pt–Co single atom alloy catalysts: accelerated water dissociation and hydrogen evolution by strain regulation, *J. Energy Chem.* 69 (2022) 44–53.
- [36] H.Q. Fu, M. Zhou, P.F. Liu, P. Liu, H. Yin, K.Z. Sun, H.G. Yang, M. Al-Mamun, P. Hu, H.-F. Wang, Hydrogen spillover-bridged Volmer/Tafel processes enabling overpotential-free current density alkaline hydrogen evolution reaction under low overpotential, *J. Am. Chem. Soc.* 144 (2022) 6028–6039.
- [37] Z. Cao, F. Dong, J. Pan, W. Xia, J.-G. Hu, X. Xu, Heteroatomic platinum–cobalt synergetic active centers with charge polarization enable superior hydrogen evolution performance in both acid and base media, *ACS Appl. Energy Mater.* 5 (2022) 1496–1504.
- [38] Y. Meng, D. Gu, F. Zhang, Y. Shi, H. Yang, Z. Li, C. Yu, B. Tu, D. Zhao, Ordered mesoporous polymers and homologous carbon frameworks: amphiphilic surfactant templating and direct transformation, *Angew. Chem. Int. Ed.* 44 (2005) 7053–7059.
- [39] J. Shim, J. Lee, Y. Ye, J. Hwang, S.-K. Kim, T.-H. Lim, U. Wiesner, J. Lee, One-pot synthesis of intermetallic electrocatalysts in ordered, large-pore mesoporous carbon/silica toward formic acid oxidation, *ACS Nano* 6 (2012) 6870–6881.
- [40] B. Liu, H. Yao, W. Song, L. Jin, I.M. Mosa, J.F. Rusling, S.L. Suib, J. He, Ligand-free noble metal nanocluster catalysts on carbon supports via “soft” nitriding, *J. Am. Chem. Soc.* 138 (2016) 4718–4721.
- [41] J. Chen, M. Aliasgar, F.B. Zamudio, T. Zhang, Y. Zhao, X. Lian, L. Wen, H. Yang, W. Sun, S.M. Kozlov, Diversity of platinum-sites at platinum/fullerene interface accelerates alkaline hydrogen evolution, *Nat. Commun.* 14 (2023) 1711.
- [42] C.-Y. Kwon, J.-Y. Jeong, J. Yang, Y.S. Park, J. Jeong, H. Park, Y. Kim, S.M. Choi, Effect of copper cobalt oxide composition on oxygen evolution electrocatalysts for anion exchange membrane water electrolysis, *Front. Chem.* 8 (2020), 600908.
- [43] G. Kresse, J. Furthmüller, Efficient iterative schemes for ab initio total-energy calculations using a plane-wave basis set, *Phys. Rev. B* 54 (1996) 11169.
- [44] J.P. Perdew, K. Burke, M. Ernzerhof, Generalized gradient approximation made simple, *Phys. Rev. Lett.* 77 (1996) 3865.
- [45] S. Grimme, Semiempirical GGA-type density functional constructed with a long-range dispersion correction, *J. Comput. Chem.* 27 (2006) 1787–1799.
- [46] S. Grimme, J. Antony, S. Ehrlich, H. Krieg, A consistent and accurate ab initio parametrization of density functional dispersion correction (DFT-D) for the 94 elements H–Pu, *J. Chem. Phys.* 132 (2010), 154104.
- [47] G. Kresse, D. Joubert, From ultrasoft pseudopotentials to the projector augmented-wave method, *Phys. Rev. B* 59 (1999) 1758.
- [48] P. Pulay, Convergence acceleration of iterative sequences. The case of SCF iteration, *Chem. Phys. Lett.* 73 (1980) 393–398.
- [49] K. Mathew, R. Sundararaman, K. Letchworth-Weaver, T. Arias, R.G. Hennig, Implicit solvation model for density-functional study of nanocrystal surfaces and reaction pathways, *J. Chem. Phys.* 140 (2014) 0804106.
- [50] G. Henkelman, B.P. Uberuaga, H. Jónsson, A climbing image nudged elastic band method for finding saddle points and minimum energy paths, *J. Chem. Phys.* 113 (2000) 9901–9904.
- [51] G. Henkelman, H. Jónsson, Improved tangent estimate in the nudged elastic band method for finding minimum energy paths and saddle points, *J. Chem. Phys.* 113 (2000) 9978–9985.
- [52] J.W. Park, G. Park, M. Kim, M. Han, J. Jang, Y. Yamauchi, B. Yuliarto, P. Krüger, J. Kim, N. Park, Ni-single atom decorated mesoporous carbon electrocatalysts for hydrogen evolution reaction, *Chem. Eng. J.* 468 (2023), 143733.
- [53] X. Zou, X. Huang, A. Goswami, R. Silva, B.R. Sathe, E. Mikmeková, T. Asefa, Cobalt-embedded nitrogen-rich carbon nanotubes efficiently catalyze hydrogen evolution reaction at all pH values, *Angew. Chem.* 126 (2014) 4461–4465.
- [54] J. Ma, M. Wang, G. Lei, G. Zhang, F. Zhang, W. Peng, X. Fan, Y. Li, Polyaniline derived N-doped carbon-coated cobalt phosphide nanoparticles deposited on N-doped graphene as an efficient electrocatalyst for hydrogen evolution reaction, *Small* 14 (2018) 1702895.
- [55] L.S. Oh, J.Y. Kim, H.W. Kim, J. Han, E. Lim, W.B. Kim, J.H. Park, H.J. Kim, Unveiling the enhanced electrocatalytic activity at electrochemically synthesized Pt–WO₃ hybrid nanostructure interfaces, *Chem. Commun.* 57 (2021) 11165–11168.
- [56] D. Kim, W.-G. Lim, Y. Kim, L.S. Oh, S. Kim, J.H. Park, C. Jo, H.J. Kim, J. Kang, S. Lee, Amorphous antimony oxide as reaction pathway modulator toward electrocatalytic glycerol oxidation for selective dihydroxyacetone production, *Appl. Catal. B: Environ.* 339 (2023), 123104.
- [57] S. Kim, H. Jung, W.G. Lim, E. Lim, C. Jo, K.S. Lee, J.W. Han, J. Lee, A versatile strategy for achieving fast-charging batteries via interfacial engineering: pseudocapacitive potassium storage without nanostructuring, *Small* 18 (2022) 2202798.
- [58] X.-J. He, J.-X. Feng, Q. Ren, G.-R. Li, Ni nanoparticle-decorated-MnO₂ nanodendrites as highly selective and efficient catalysts for CO₂ electroreduction, *J. Mater. Chem. A* 6 (2018) 19438–19444.
- [59] H. Huang, H. Jung, S. Li, S. Kim, J.W. Han, J. Lee, Activation of inert copper for significantly enhanced hydrogen evolution behaviors by trace ruthenium doping, *Nano Energy* 92 (2022), 106763.
- [60] S. Kim, C. Choi, J. Hwang, J. Park, J. Jeong, H. Jun, S. Lee, S.-K. Kim, J.H. Jang, Y. Jung, Interaction mediator assisted synthesis of mesoporous molybdenum carbide: Mo-valence state adjustment for optimizing hydrogen evolution, *ACS Nano* 14 (2020) 4988–4999.
- [61] H. Prats, K. Chan, The determination of the HOR/HER reaction mechanism from experimental kinetic data, *Phys. Chem. Chem. Phys.* 23 (2021) 27150–27158.
- [62] T. Shinagawa, A.T. Garcia-Esparza, K. Takanabe, Insight on Tafel slopes from a microkinetic analysis of aqueous electrocatalysis for energy conversion, *Sci. Rep.* 5 (2015) 13801.
- [63] L. Fan, P.F. Liu, X. Yan, L. Gu, Z.Z. Yang, H.G. Yang, S. Qiu, X. Yao, Atomically isolated nickel species anchored on graphitized carbon for efficient hydrogen evolution electrocatalysis, *Nat. Commun.* 7 (2016) 10667.
- [64] R.J. Isaifan, S. Ntais, E.A. Baranova, Particle size effect on catalytic activity of carbon-supported Pt nanoparticles for complete ethylene oxidation, *Appl. Catal. A: Gen.* 464 (2013) 87–94.
- [65] A. Mohsenzadeh, K. Bolton, T. Richards, DFT study of the adsorption and dissociation of water on Ni (111), Ni (110) and Ni (100) surfaces, *Surf. Sci.* 627 (2014) 1–10.
- [66] Q. Li, H. Peng, Y. Wang, L. Xiao, J. Lu, L. Zhuang, The comparability of Pt to Pt–Ru in catalyzing the hydrogen oxidation reaction for alkaline polymer electrolyte fuel cells operated at 80°C, *Angew. Chem.* 131 (2019) 1456–1460.